Polymer Chemistry

PAPER

View Article Online
View Journal | View Issue

Cite this: *Polym. Chem.*, 2019, **10**, 6010

Triazine-functionalized covalent benzoxazine framework for direct synthesis of N-doped microporous carbon†

Hesham R. Abuzeid,[a] Ahmed F. M. EL-Mahdy,[a,b] Mahmoud M. M. Ahmed[a] and Shiao-Wei Kuo *[a,c]

Received 15th August 2019,
Accepted 19th October 2019

DOI: 10.1039/c9py01231a

rsc.li/polymers

A covalent benzoxazine framework (CBF) was synthesized through a one-pot Mannich reaction of the planar molecules 1,3,5-tris(4-aminophenyl)triazine (TAPT) and 2,4,6-tris(*p*-hydroxyphenyl)triazine (THPT) with paraformaldehyde. This covalent benzoxazine framework underwent thermal curing to generate a highly cross-linked covalent benzoxazine framework (CCBF), with subsequent carbonization and KOH activation providing a nitrogen-doped microporous carbon (N-DMC)—prepared without the need for a template. This nitrogen-doped microporous carbon possessed a spherical morphology, excellent thermal stability (with a T_{d5} value of 663 °C and a char yield of 85%), a high BET surface area (1469 $m^2\ g^{-1}$), and a pore size of 2.07 nm. The thermal transformations from the CBF to the CCBF and then to N-DMC enhanced the CO_2 capture ability and electrochemical capacitance. The nitrogen-doped microporous carbon displayed excellent CO_2 capture capacities of 3.85 and 7.46 mmol g^{-1} at 298 and 273 K, respectively; moreover, it provided an electrochemical capacitance of 185 F g^{-1} at a current density of 1.0 A g^{-1}, as well as excellent stability (average capacitance retention of 87% at 20 A g^{-1} after 4000 cycles).

Introduction

Benzoxazines (BZs) are interesting monomers that are prepared through Mannich condensations of amines and phenolic derivatives.[1–5] They undergo ring opening polymerizations under mild conditions, and in the absence of strong chemical agents, to form polybenzoxazines. In general, BZ monomers have been prepared using mono- or bi-functionalized phenolic and amino derivatives to form the low-molecular-weight compounds or main chain – type BZ prepolymers that typically impart valuable mechanical and thermal properties (*e.g.*, high char yields and glass transition temperatures, low dielectric constants, and low surface free energies).[6–8] To increase the thermal stability of polybenzoxazines by composited with inorganic materials including carbon and silica based nanomaterials have been proposed.[9–14]

Moreover, the ring opening reaction of benzoxazine originating from the curing step yielded a big family of carbonized materials with various pore sizes and distributions.[15–25] These obtained carbonized products opened the door for further applications of activated polybenzoxazines in various fields. In other words, these motivating simple chemical reactions and excellent properties induced more values to polybenzoxazine[15–25] and further studies have been performed on the activated carbons derived from polybenzoxazines. These activated carbons were widely used in various applications through either composite formation with benzoxazines or completely converting them into active carbons. The activated carbons obtained upon thermally curing benzoxazines attracted much attention in various applications.[15–25]

Several methods have been developed for the synthesis of N-doped porous carbons, including (i) co-carbonizations of N-free precursors with N-containing materials, (ii) reactions of N-containing materials (*e.g.*, melamine) with porous carbon, and (iii) direct carbonizations of raw-N containing materials.[26–29] These N-doped porous carbon materials often display excellent CO_2 uptake properties and excellent electrochemical performance; they have been prepared from well-known N-containing thermoplastic polymers, including polyaniline, polypyrrole, and polyacrylonitrile, as the carbon precursors.[30–32] Polybenzoxazines are thermoset resins that also possess N atoms; they undergo carbonization to give

[a]*Department of Materials and Optoelectronic Science, Center of Crystal Research, National Sun Yat-Sen University, Kaohsiung 80424, Taiwan.*
E-mail: kuosw@faculty.nsysu.edu.tw
[b]*Chemistry Department, Faculty of Science, Assiut University, Assiut 71516, Egypt*
[c]*Department of Medicinal and Applied Chemistry, Kaohsiung Medical University, Kaohsiung, 807, Taiwan*

†Electronic supplementary information (ESI) available: Details of synthetic approaches and materials characterizations. See DOI: 10.1039/c9py01231a

N-doped porous carbon materials that can exhibit thermal properties superior to other N-containing thermoplastic polymers.[15–25] For example, Hao *et al.* developed the poly (benzoxazine-*co*-resol) polymer to synthesize N-doped porous carbon, which display both good CO_2 uptake ability and electrochemical performance.[15,16] The formations of nitrile-functionalized benzoxazines—using 4-cyanophenol as a phenolic precursor—followed by thermal trimerization of nitrile groups and ring-opening of benzoxazine rings have been reported as another method to prepare N-doped porous carbons. Li and co-workers have reported using 4-cyanophenol, melamine and formaldehyde to synthesize nitrile-functional benzoxazine *via* a solution method. Then the resultant benzoxazine underwent ring-opening polymerization followed by calcination and KOH activation to produce nitrogen-containing porous carbons.[20,21] We used 4-cyanophenol, 1,3,5-tris(4-aminophenoxy)benzene, and CH_2O to form the nitrile-functionalized benzoxazine matrix and then obtained the N-doped microporous carbon. Because of the increase of the N atom concentration after the formation of triazine units by thermal curing, it displayed better CO_2 uptake ability.[33] However, trimerization of the corresponding aromatic nitriles under thermal conditions usually suffers from numerous disadvantages such as the long reaction time and the onerousness to remove the unconverted nitrile monomer from the product. Therefore, there is still interest in the formation of N-doped porous carbons from triazine-based benzoxazine without thermal trimerization of the nitrile group.

The strategic design of microporous polymer frameworks (MPFs), in which the building units are connected through covalent bonds, is receiving significant attention because of their potential applications.[34–37] These MPFs feature either two-dimensional (2D) or three-dimensional polymeric frameworks, for example, covalent triazine, metal–organic, and covalent organic frameworks (COFs), which have diverse pore size distributions.[38–43] Insertion of heteroatoms (*e.g.*, N) into the frameworks of MPFs—by employing various heteroatom-containing building units and controlling their pore sizes through the selection of building units of various sizes—can greatly enhance their CO_2 adsorption behavior and electrochemical performance.[44–48] However, the design and synthesis of microporous polymeric frameworks based on the important benzoxazine moiety have not been reported yet. Therefore, this is the first study to use both tri-functionalized phenolic and amine linkers based on the triazine unit to form the new covalent benzoxazine framework (CBF). Upon thermal treatment, nitrogen-doped microporous carbon (N-DMC) could be synthesized through the ring-opening curing of the CBF followed by calcination, treated with KOH and reheated under a N_2 atmosphere, as displayed in Scheme 1. This activated nitrogen-doped microporous carbon exhibits a high surface area and less defective graphitic structure with a high concentration of N atoms from both the benzoxazine ring and the triazine units. Moreover, this nitrogen-doped microporous carbon provided an exceptional CO_2 adsorption and efficient electrochemical energy storage and thus it provides a new route for the development of polymeric materials in reducing the global energy crisis.

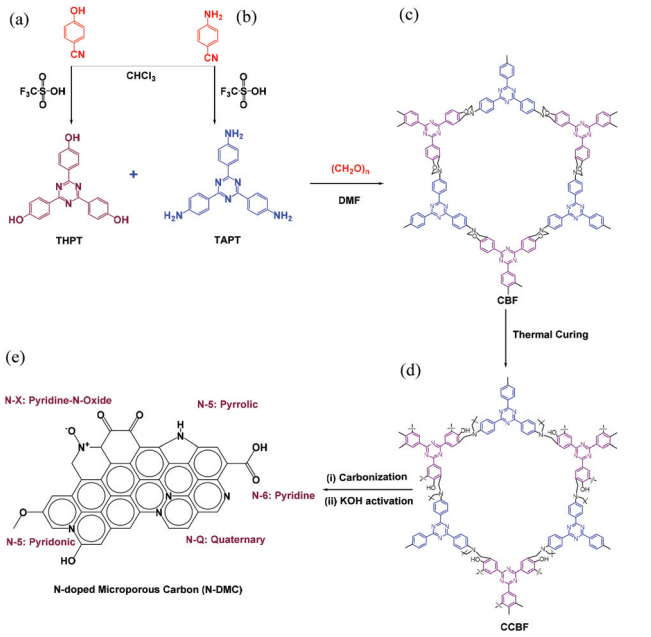

Scheme 1 Synthesis of (a) TAPT and (b) THPT and their Mannich reaction to give (c) CBF. (d) Formation of the CCBF through thermal curing. (e) Carbonization and activation with KOH giving the N-DMC.

Experimental section

Materials

4-Aminobenzonitrile, 4-hydroxybenzonitrile, trifluoromethane sulfonic acid (TfOH), paraformaldehyde, ammonium hydroxide, chloroform, dimethylformamide (DMF), and all other chemicals were purchased from Sigma-Aldrich.

1,3,5-Tris(4-aminophenyl)triazine (TAPT)

This compound was synthesized according to previously reported methods,[49] through trimerization of 4-aminobenzonitrile with TfOH as the catalyst (Scheme S1†). A solution of 4-aminobenzonitrile (3.09 g, 26.1 mmol) in $CHCl_3$ (40 mL) was placed in a round-bottom flask at 0 °C. TfOH (8.00 mL, 30.4 mmol) was added dropwise over 15 min while maintaining the temperature at 0 °C. The mixture was stirred at room temperature for 24 h under a N_2 atmosphere. Ice-cooled distilled H_2O (50 mL) was added and then the mixture was neutralized by adding 2 M NH_4OH until the pH exceeds 7. Initially, upon increasing pH, the orange precipitate dissolved to give a bright-orange solution. A further increase in pH provided a pale-yellow precipitate, which was filtered off and then washed three times with distilled H_2O and MeOH. The solvent was evaporated slowly through using vacuum distillation. The residue was dried in a vacuum oven to provide a pale-yellow powder (2.81 g, 91%). FTIR (KBr, cm^{-1}): 3463, 3377, 3320, 13 212, 3029, 1633, 1607, 1579, 1500. ^1H NMR (500 MHz,

DMSO-d_6, ppm): δ 8.35 (d, J = 8.95 Hz, 6H), 6.69 (d, J = 8.95 Hz, 6H), 5.90 (s, 6H).

2,4,6-Tris(4-hydroxyphenyl)triazine (THPT)

TfOH (3.8 mL) was added carefully to a solution of 4-cyanophenol (1.00 g, 8.39 mmol) in $CHCl_3$ (20 mL) at 0 °C and then the mixture was left for 30 min at 0 °C and 18 h at room temperature (Scheme S2†). Ice-cooled distilled H_2O (50 mL) was added and then the mixture was neutralized by adding 2 M NH_4OH until the pH exceeded 7. Upon increasing the pH, the red solution produced an off-white precipitate, which was filtered off and dissolved in acetone. After adding water, the precipitate was filtered off and placed in a vacuum oven at 100 °C to give an off-white solid (0.93 g, 93%). FTIR (KBr, cm^{-1}): 3545–3120, 1143, 1633, 1579, 1500, 3029, 3045. ^{1}H NMR (500 MHz, DMSO-d_6, ppm): δ 8.54 (d, J = 9.0 Hz, 6H), 6.97 (d, J = 8.5 Hz, 6H), 10.28 (s, 3H).

Covalent benzoxazine framework (CBF) and cross-linked CBF (CCBF)

A solution of paraformaldehyde (0.102 g, 3.40 mmol), TAPT (200 mg, 0.559 mmol), and THPT (198.35 mg, 0.559 mmol) in DMF (20 mL) was heated at 100 °C under N_2 for 48 h. The precipitate was washed with MeOH and filtered. Then it was soaked in MeOH, THF, and acetone for 3 days while changing solvents every 8 h (Scheme S3†). The sample CBF was dried in a vacuum oven at 60 °C to provide a yellow powder. A desired amount of CBF was charged in an aluminum pan and heated at 240 °C for 2 h in an oven to form the CCBF (Scheme S4†).

N-Doped microporous carbon (N-DMC)

After thermal curing, the product was calcined under a N_2 atmosphere in a tubular furnace at temperatures from 25 to 600 °C at a heating rate of 5 °C min^{-1} and then maintained at 600 °C for 6 h. The mixture was then treated with aqueous KOH (carbon/KOH = 1/2 by weight ratio) and stirred for 24 h at room temperature. After evaporating H_2O, the carbon powder was further activated at 800 °C in a tubular furnace for 2 h under a N_2 atmosphere. The product was washed several times with deionized H_2O until the pH reached 7 and then dried overnight at 120 °C to yield the CCBF activated black powder (Scheme S5†).

Results and discussion

A new covalent benzoxazine framework was synthesized *via* a solvothermal method using trifunctional aminophenyl triazine (TAPT) and trifunctional hydroxyphenyl triazine (THPT) with paraformaldehyde through the Mannich condensation reaction. In order to get rid of the unreacted monomers, the resultant CBF was sequentially washed with methanol, THF, and finally with acetone for 3 days. We confirmed the successful synthesis of both TAPT and THPT monomers by NMR and FTIR spectroscopy. Fig. 1 displays the ^{1}H NMR spectra of both samples. Two doublets appeared at 8.54 and 6.97 ppm with an integrated ratio of 1 : 1, corresponding to the aromatic CH protons of THPT (Fig. 1a); the signal of the OH group appeared at 10.28 pm. The spectrum of TAPT (Fig. 1b) also featured two doublets at 8.35 and 6.69 ppm, also with the integrated ratio of 1 : 1, assigned to the aromatic CH protons of TAPT; the protons of the NH_2 group appeared as a signal at 5.90 ppm. Fig. 2 presents the FTIR spectra, recorded at room temperature, of TAPT, THPT and CBF. The characteristic N–H stretching vibrations of TAPT appeared (Fig. 2a) as bands at 3463, 3377, 3320, and 3212 cm^{-1}; the signal for N–H bending appeared at 1607 cm^{-1}; and the signal for C–N vibration appeared at 1177 cm^{-1}. The spectrum of THPT featured signals for the O–H groups at 3545–3120 cm^{-1} and for the C–O units at 1143 cm^{-1}. The characteristic adsorption peaks of the triazine moiety appeared at 1633 (C=N), 1579 and 1500 (C=C), and 3029 and 3045 (aromatic C–H stretching) cm^{-1} (Fig. 2b). The signals for the NH_2 (*ca.* 3545–3120 cm^{-1}) and OH (3463–3320 cm^{-1}) groups were strongly attenuated after the condensation process; new peaks appeared at 1226 (C–O stretching) and 921 (benzoxazine ring) cm^{-1}, suggesting a high degree of polymerization for the CBF (Fig. 2c).[1,2] Due to

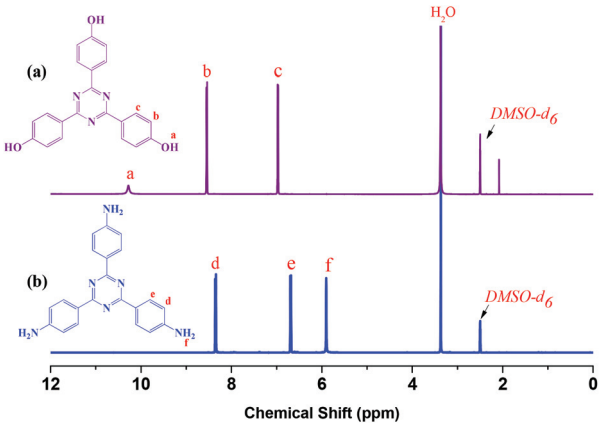

Fig. 1 ^{1}H NMR spectra of triazine monomers: (a) THPT and (b) TAPT.

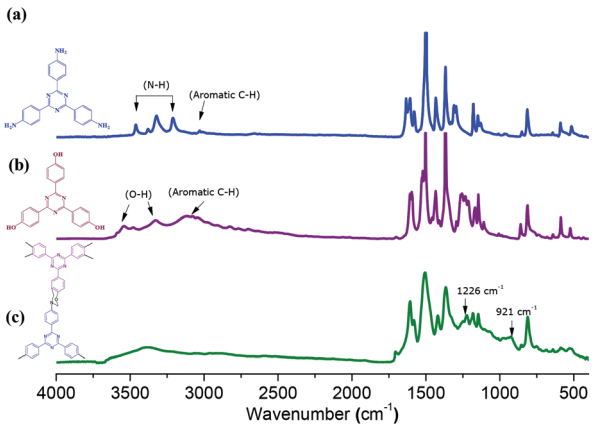

Fig. 2 FTIR spectra of the triazine monomers: (a) TAPT and (b) THPT; covalent benzoxazine framework, CBF (c).

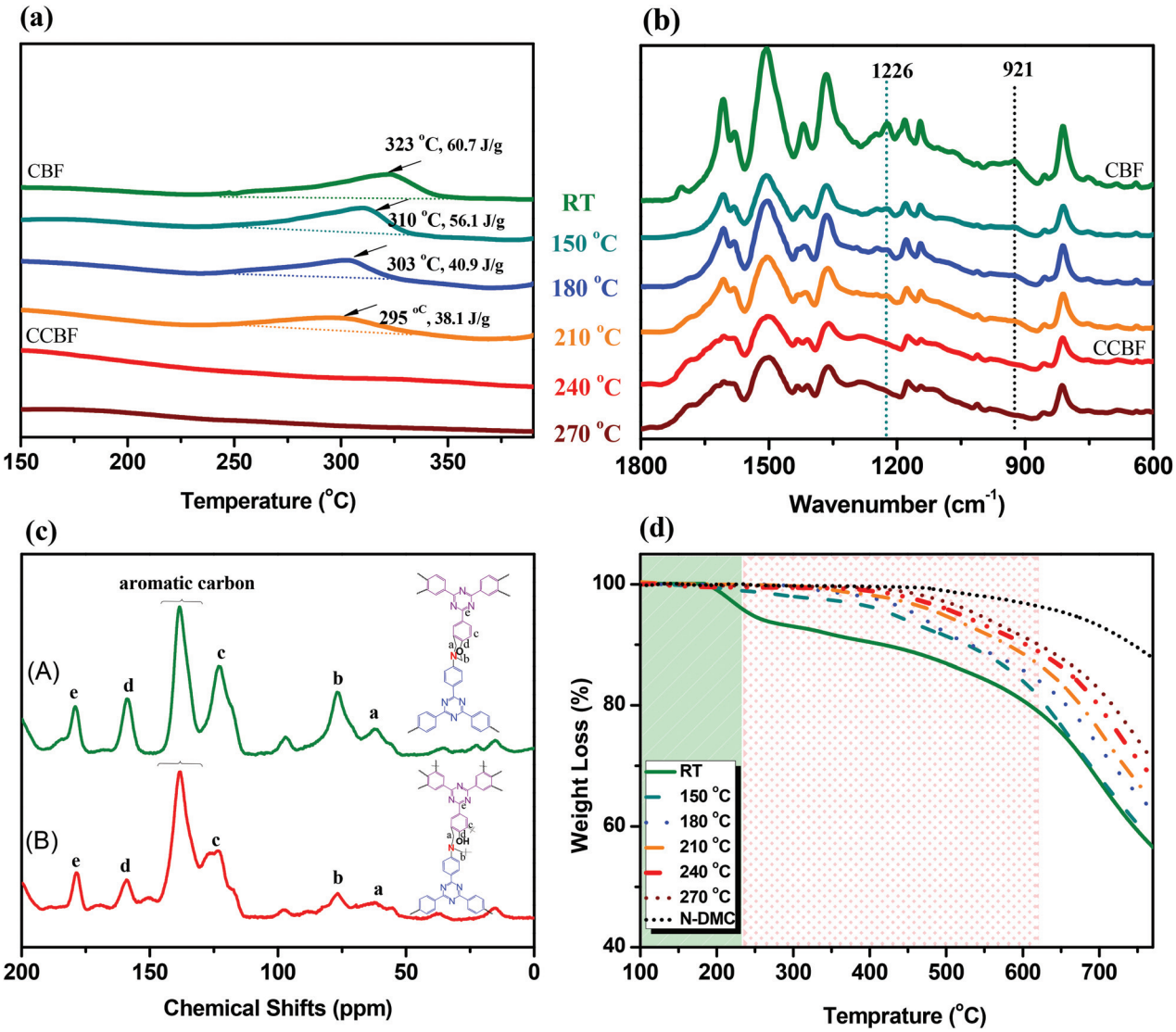

Fig. 3 (a) DSC and (b) FTIR spectral analyses of the CBF before and after thermal curing at various temperatures. (c) Solid-state ^{13}C NMR spectra of the CBF (A) and CCBF (B). (d) TGA thermograms of the CBF at room temperature, after thermal curing at 150, 180, 210, 240, and 270 °C and after KOH activation (N-DMC) under a N_2 atmosphere.

the lack of solubility of our synthesized CBF in common NMR solvents, we thus used the solid state ^{13}C NMR to determine the chemical structure of the CBF as displayed in Fig. 3(c). Two characteristic peaks at 59.9 and 76.4 ppm were corresponding to the CCH_2N (peak a) and OCH_2N (peak b) benzoxazine ring of the CBF and the other aromatic and C═N showed triazine ring signals from 122.8 to 178.8 ppm (Fig. 3c-A). In addition, thermal curing of the formed CBF was performed at 240 °C for 2 h to produce the highly cross-linked CBF (CCBF) through ring-opening polymerization of the benzoxazine rings. Solid-state NMR spectra were also collected to confirm the structure of the CCBF as displayed in Fig. 3c-B. The spectrum featured strong peaks from 122.8 to 178.8 ppm which correspond to the aromatic carbon and C═N in triazine rings. Moreover, the characteristic peak of benzoxazine ring carbons at 76.4 ppm and 59.9 was significantly attenuated and new peaks were observed at 76.2 and 62.3 ppm (peaks a and b in Fig. 3c-B), corresponding to the methylene units after thermal curing. As a result, we conclude that the tri-functionalized triazine-based monomers (TAPT and THPT), CBF, and CCBF were synthesized successfully with a high degree of purification. We investigated the dynamic thermal curing behavior at different temperatures for CBF-1 by combining DSC and FTIR analyses. Fig. 3a displays the DSC thermograms of the CBF before and after thermal curing at various temperatures. An exothermic peak was observed at 323 °C with the thermal curing enthalpy of 60.07 J g^{-1}. These two values exhibited a gradual decrease upon increasing the thermal curing temperature from 150 to 210 °C, implying the increase of the ring-opening extent for the CBF, while this exothermic peak totally disappeared after

the thermal curing at 240 °C, indicating the completely thermal curing of the CBF and its conversion into the cross-linked CCBF. Furthermore, we performed FTIR analysis to monitor the thermal curing behavior of the CBF under the same thermal curing conditions as shown in Fig. 3b. This characteristic absorption band of the benzoxazine ring appeared at 921 and 1226 cm^{-1} and these two peaks greatly decreased with the increase of curing temperature, which almost disappeared after thermal curing at 240 °C, as displayed in Fig. 3b.[50] FTIR analysis is consistent with the DSC result as confirmed by the benzoxazine ring-opening and formation of the CCBF that occurred at 240 °C.

We used TGA to study the thermal curing, carbonization, and activation of the CBF under a N_2 atmosphere. All samples exhibited high thermal stability at temperatures up to 800 °C, with char yields greater than 52 wt%. As displayed in Fig. 3(d) for the TGA curve of the CBF before curing, a low weight loss (6.9 wt%) occurred at temperatures in the range of 200–260 °C, representing the ring opening of the BZ structure. A second weight loss of 14.9 wt%, corresponding to framework carbonization and decomposition of the N species, occurred upon heat treatment at temperatures between 260 and 630 °C. The highest weight loss of 29.1 wt% occurred at temperatures above 630 °C, corresponding to further release of C and N atoms in the forms of gaseous products. Finally, a carbon residue of 52 wt% remained after heating at 800 °C. Hence, both the thermal decomposition temperature (T_{d5}) and the char yield underwent a gradual increase after thermal curing from 150 to 270 °C, because of the increase in the cross-linking density [Fig. 3(d)].

Moreover, the TGA curves of the CBF after activation displayed a negligible weight loss at temperatures below 500 °C, followed by a gradual loss of 11.3 wt% at temperatures between 500 and 800 °C; the char yield remained as high as 85 wt%, presumably because of the existence of fused rings in the CBF having a rigid framework, with the CBF 2D framework further extending and then improving the cross-linking density.

The wide-angle X-ray diffraction (WAXD) pattern of the CBF [Fig. 4(a), olive line] is characterized by diffraction peaks at a q ratio of $1:\sqrt{4}:\sqrt{7}:\sqrt{9}$, revealing that it maintained a highly ordered hexagonally packed cylindrical structure [see the inset to Fig. 4(a)], as well as a sharp diffraction peak at a value of 2θ of 4.43° (d = 1.51 nm), corresponding to the (100) reflection. Material Studio software was used to perform the structural modeling and obtain theoretical WAXD simulated patterns of the CBF in addition to predicting the WAXD simulated patterns for the stacked structures. We found that the experimental WAXD reflection of the CBF matched well with the theoretical pattern (violet curve) and also differed negligibly (black curve) from the structural simulation of the AA-eclipsed layer stacking mode (red curve) (Fig. S1–3, Table S1†). Furthermore, the patterns of the CCBF and N-DCM (Fig. S2†) featured diffraction peaks identical to those of the CBF; these samples also featured extra diffraction peaks at higher values of q, representing a d-spacing of 0.41 nm that presumably corresponds to the inter-layer distance between the highly ordered hexagonal packing layers. The Brunauer–Emmett–Teller (BET) surface areas of the CBF, CCBF, and N-DMC revealed typical type-IV adsorption isotherms with noticeable H_4-type hysteresis loops in the relative pressure (P/P_0) region of 0.7–1.0, suggesting the coexistence of mesopores and micropores in these samples [Fig. 4(b)]. The sharp rise in the N_2 isotherm of N-DCM was observed at a relatively low pressure (P/P_0 = 0–0.01), revealing the high surface area and the existence of large amounts of micropores. The CBF featured a BET surface area of 71.8 $m^2\ g^{-1}$; it increased slightly after thermal curing, reaching 86.4 $m^2\ g^{-1}$ for the CCBF. In contrast, the N-DMC possessed a significantly greater BET surface area of 1469 $m^2\ g^{-1}$, revealing the importance of the activation process in enhancing the surface area. The inset to Fig. 4(b) displays the pore size distribution curves determined from the N_2 adsorption/desorption isotherms. We used the NL-DFT method to determine the pore size distribution of the CBF, CCBF, and N-DMC, indicating that the pore diameters are 2.72, 2.26, and 1.43 nm, respectively. Table 1 lists the BET surface areas and pore volumes of these samples; we conclude that the N-DCM possessed the highest surface area because a high volume of fine micropores (pore size: *ca.* 1.43 nm) formed during its activation process at higher temperature. Das *et al.*[51] reported the synthesis of viologen-based covalent organic frameworks (HS and HT) with BET surface areas of 12 and 35 $m^2\ g^{-1}$, respectively. The low values of these BET surface areas have been interpreted to the occupation of COF pores with chloride ions. Tilford *et al.*[52] also reported the synthesis of the alkylated COF (COF-11) with a BET surface area of 105 $m^2\ g^{-1}$. They explained that the alkyl group could create a pore corner cavity, which prohibited the access of N_2 to the pore corners. These reports indicated that there are different reasons for reducing the surface area for the framework materials. Therefore, with our synthesized CBF and CCBF, the low BET surface areas of these materials can be attributed to the flexible structure of the benzoxazine ring and the presence of Mannich methylene bridges after thermal curing, which might block the access of nitrogen to the pore corners. We used field-emission scanning electron microscopy (FE-SEM) and transmission electron microscopy (TEM) to investigate the morphologies of the N-doped microporous carbons. As displayed in Fig. 4(c), the FE-SEM image of the synthesized N-DMC revealed a spherical morphology with diameters of approximately 80–100 nm. The majority of these spheres presented a set of sheaves; some individual spheres were, however, present, due to the long period of sonication applied during the sample preparation. The morphology of the N-DMC was confirmed using TEM, which revealed the assembly of homogenous dark spheres of the N-DMC having a smooth outer surface. Statistical analysis of these spheres indicated that the average diameter of the spheres was 80–100 nm. We attribute the formation of this spherical N-DMC to thermal cross-linking of the BZ rings in the CBF to form the CCBF, which, after carbonization and KOH activation, exhibited no loss in stability. The local graphitic structure of the N-doped

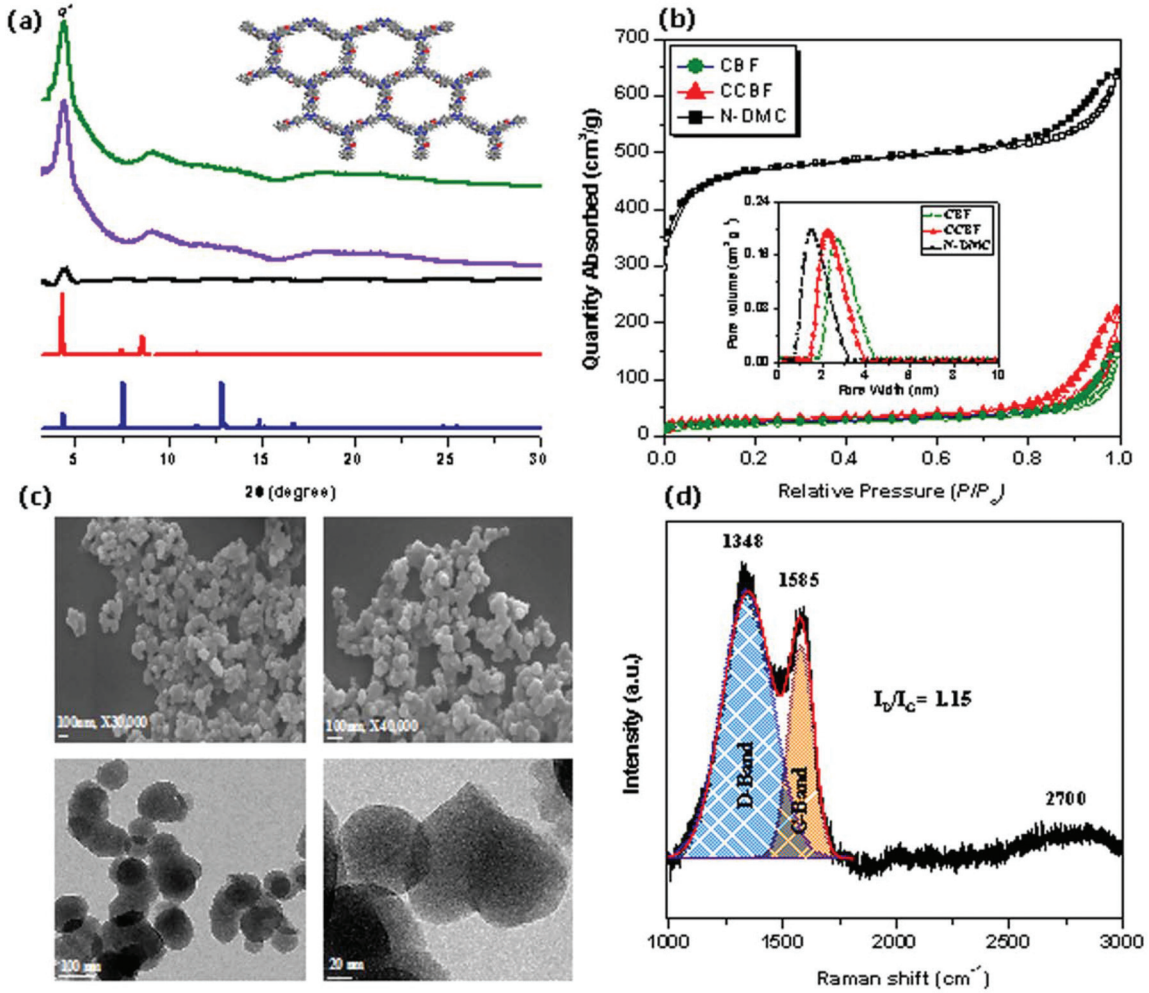

Fig. 4 (a) WAXD profiles of the CBF: experimentally observed (olive); Pawley refined (violet); difference between the simulated and calculated data (black); calculated for the hexagonally structure AA-stacking model (red); corresponding hexagonal simulated structure for the CBF. (b) N_2 adsorption/desorption isotherms and pore size distribution curves determined at 77 K for the CBF, CCBF, and N-DMC. (c) FE-SEM and TEM images of the spherical N-DMC, measured at various magnifications. (d) Raman spectrum of the N-DMC.

Table 1 Thermal stability, BET surface area, and CO_2 capture for CBF derivatives

Samples	T_{d5} (°C)	Char yield (wt%)	S_{BET} ($m^2\ g^{-1}$)	S_{micro} ($m^2\ g^{-1}$)	CO_2 uptake (mmol g^{-1}) 0 °C	25 °C
CBF	245	52	71.8	9.88	1.88	1.48
CCBF	519	65	86.4	12.58	2.35	1.93
N-DMC	663	85	1469	988.89	7.46	3.85

microporous carbons was observed using Raman spectroscopy. Fig. 4(d) shows a major carbonized structure with two identical D and G bands, corresponding to the sp^3- and sp^2-hybridized carbon atoms, respectively. The D-band, appearing at 1347.9 cm^{-1}, represents second-order Raman scattering; the G-band, at 1584.6 cm^{-1}, represents first-order Raman scattering.[53] This G-band position reveals a major shift in the Fermi energy level of this N-DMC relative to other carbon materials (*e.g.*, graphene), which usually exhibits a G-band at 1582 cm^{-1} with zero band gap. Moreover, this position of a single G-band without splitting also suggests the mild doping of the oxidative species into the carbon skeleton, relative to that of oxidized graphene with its G-bands positioned near 1590 and 1625 cm^{-1}. The peak intensity ratio I_D/I_G was equal to 1.15, indicating the existence of abundant defects, due to successful hybridization of the carbon structure with N and O atoms after soaking with KOH and then heating under an inert atmosphere. As a result, the activation process created functionalized carbon structures, more so than graphitic structures, and the minor 2D bands near 2700 cm^{-1} appeared as the double of the D-band position as a first-order Raman scattering. These characteristic bands revealed the successful conversion of the CBF after the activation process with a clear graphitic structure.

We applied X-ray photoelectron spectroscopy (XPS) to investigate the amounts of N and O species at the CCBF and

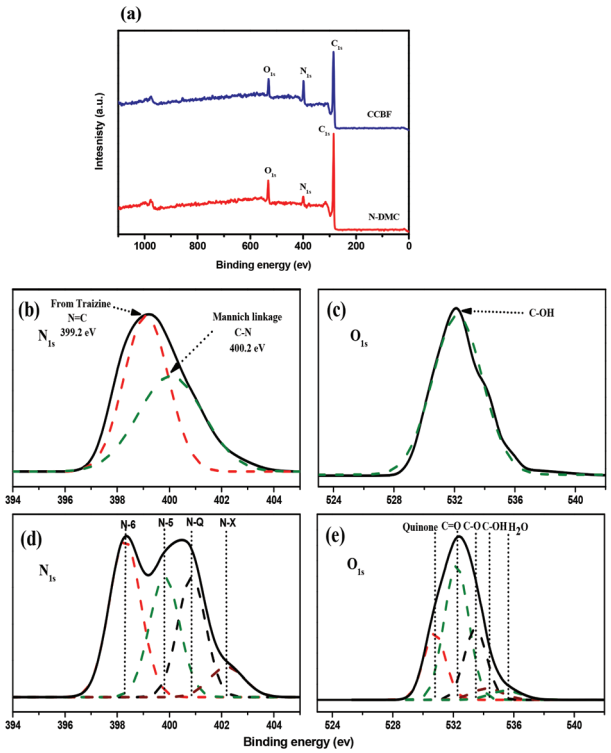

Fig. 5 (a) XPS spectra of the CCBF and N-DMC and N_{1s} and O_{1s} orbitals of the CCBF (b and c) and (d and e) N-DMC samples.

N-DMC surfaces [Fig. 5(a)]. The N content for N-DMC was lower than that for the CCBF; we observed N (14.8 and 6.8 wt%, respectively), O (6.1 and 9.2 wt%, respectively), and C (79.1 and 84.0 wt%, respectively) atoms for both the CCBF and N-DMC. The XPS spectra of the N_{1s} orbitals could be deconvoluted into two peaks for the CCBF: at 399.2 and 400.2 eV for nitrogen in the triazine ring and Mannich linkage (NCH_2N), respectively.[54,55] Furthermore, four peaks were observed for N-DMC: at 398.3 [pyridine-N (N-6)], 399.8 [pyrrole-nitrogen or pyridone-nitrogen (N-5)], 400.9 [quaternary-N (N-Q)], and 402.2 eV [pyridine-N-oxide (N-X)], as displayed in Fig. 5(b) and (d) and Scheme 1(e). Table 2 presents the content of each atom of the N-DMC, revealing the high concentrations of N-6, N-Q, and N-X; there was, however, an obvious decrease in the concentration of N-5. It has been reported that N-Q units have superior thermal stability when compared to other N functionalities.[56,57] The N-6 and N-5 atoms could take part in reversible pseudofaradaic redox reactions. Hence, an electrochemically active pseudocapacitance effect would appear when using an alkaline aqueous electrolyte. Moreover, the N-6 atoms, adjacent to two C atoms in the graphitic sp^2-hybridized network, underwent strong hydrogen bonding with surrounding C–H bonds. For the pyridonic-N atom, the p-orbital could provide a p–p conjunction effect with the p-bond in its –OH unit and improve its Lewis basicity. As a result, the pyridonic-N atoms in N-5 and N-6 displayed Lewis basicity stronger than the other N functionalities; thus, these bonds played important roles in enhancing the CO_2 capture ability. Interestingly, the N-5 and N-6 atoms represented more than 66% of the total N species in the N-DMC. Such an N-DMC, rich in N-5 and N-6 atoms, is a desirable material for high-performance CO_2 capture and for preparing electrodes. In addition, the O_{1s} curve could also be resolved into a major peak at 532.2 eV (C–OH) for CCBF[58] and five signals for O-containing functional units in N-DMC at 530.7 (quinone), 532.2 (C═O), 533.5 (C–O), 534.2 (C–OH), and 535.5 eV (adsorbed H_2O), as displayed in Fig. 5(c) and (e). It has been reported that, in an alkaline medium, the C–O and quinone units in a C matrix are not electrochemically active during the reversible redox reaction.[59] Nevertheless, the reduction of phenolic-hydroxyl (C–OH) units and the deprotonation of carboxylic (C═O) groups led to a quasi-reversible pseudocapacitance. Fortunately, the content of C–OH and C═O units was greater than 52% of the total of the O species in the N-DMC, potentially making the N-DMC a suitable electrode material for measuring the total capacitance.

We used our samples as adsorbents to investigate their CO_2 capture ability. The CO_2 adsorption isotherms of the CBF, CCBF, and N-DMC were determined at 25 and 0 °C under atmospheric pressure [Fig. 6(a) and (b)]. The CBF and CCBF possessed the low surface areas of 71.8 and 86.4 $m^2\ g^{-1}$, respectively; thus, they exhibited relatively low degrees of CO_2 capture of 1.48 and 1.98 mmol g^{-1}, respectively, at 25 °C and 1.88 and 2.35 mmol g^{-1}, respectively, at 0 °C. These values increased dramatically after carbonization and activation to give the N-DMC; with a much higher surface area of 1469 $m^2\ g^{-1}$, the CO_2 uptakes were significantly higher at 3.85 and 7.46 mmol g^{-1} at 25 and 0 °C, respectively. Such great improvements can be explained by considering the high N atom concentrations arising originally from the triazine and BZ units and the high surface area, as well as the acidity of CO_2 gas. This observation was supported by the calculation of the isosteric heats of adsorption (Q_{st}) of the CBF, CCBF, and N-DMC, from the CO_2 adsorption data measured at 25 and 0 °C, according to the Clausius–Clapeyron equation. Fig. 6(c) presents the fitting isotherms of the CBF, CCBF, and N-DMC. By taking a low loading of CO_2 (0.1 mmol g^{-1}) as a standard, the CBF, CCBF, and N-DMC provided Q_{st} values of 38.92, 40.35, and 80.25 kJ mol^{-1}, respectively. These values indicate

Table 2 Curve fitting result of N_{1s} and O_{1s} spectra

	XPS analysis			N species				O species				
Samples	C	O	N	N-6	N-5	N-Q	N-X	Quinone	C═O	C–O	C–OH	H_2O
N-DMC	84.0	9.2	6.8	38.05	27.98	25.88	8.08	20.97	47.00	22.90	4.99	4.12

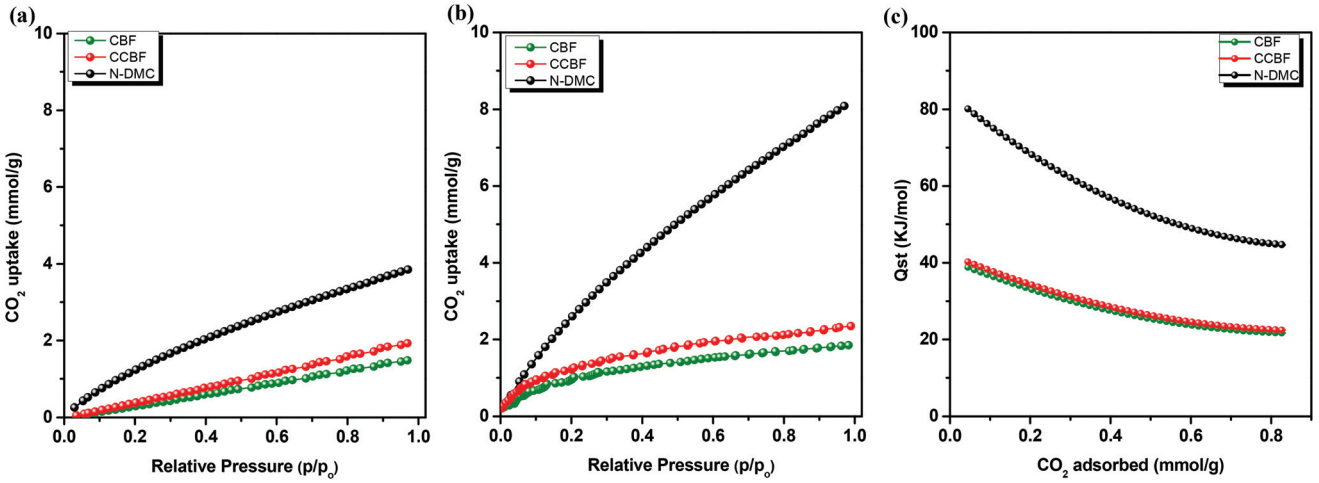

Fig. 6 (a and b) CO_2 uptake profiles of the CBF, CCBF, and N-DMC at (a) 25 and (b) 0 °C. (c) Isosteric heats of adsorption (Q_{st}) for the CBF, CCBF, and N-DMC, obtained from the CO_2 uptake isotherms collected at 25 and 0 °C.

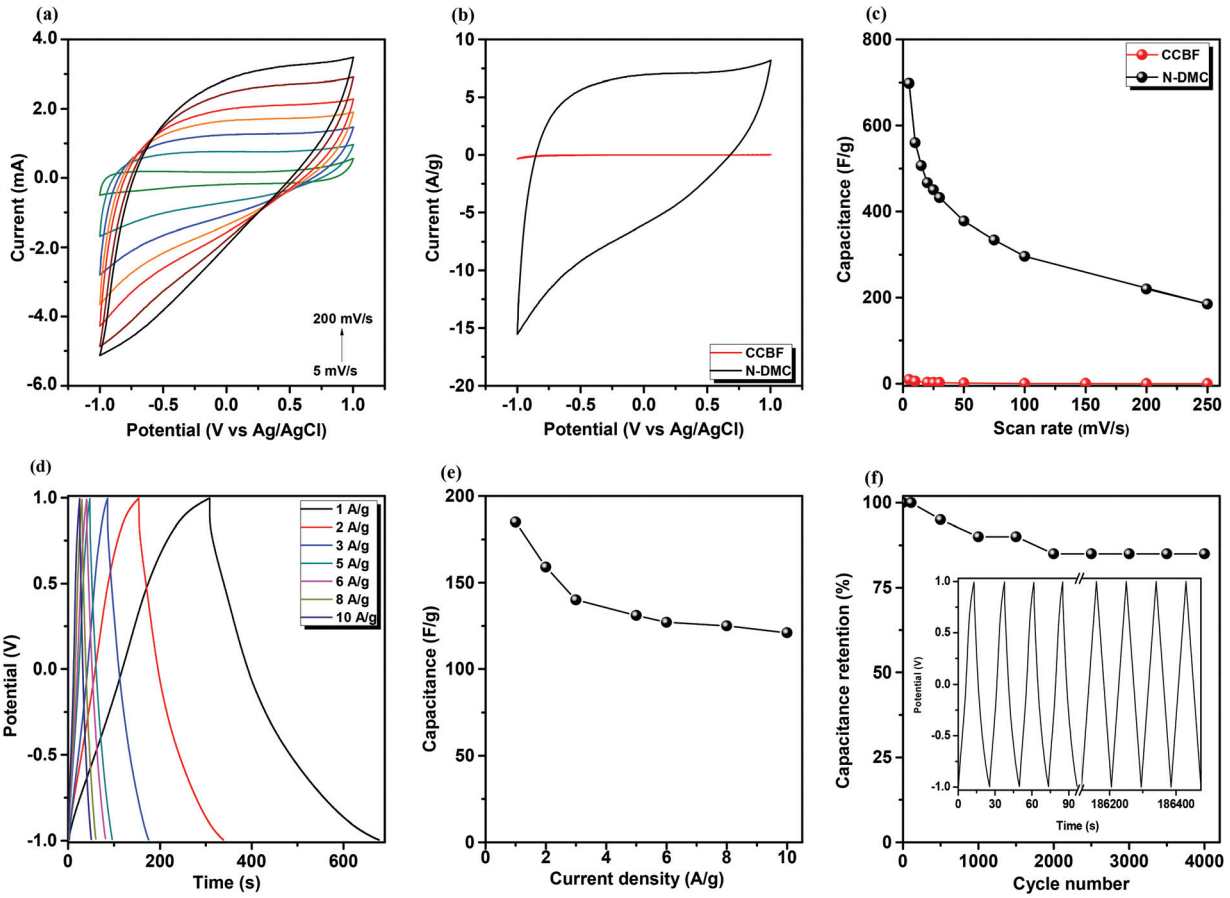

Fig. 7 (a) CV curves of the N-DMC measured at various scan rates. (b) Comparison of the CV curves of the CCBF and N-DMC. (c) Capacitance plotted with respect to the scan rate for both the CCBF and N-DMC at 50 mV s^{-1}. (d) Charge/discharge curves of the N-DMC measured at various current densities. (e) Capacitance plotted with respect to the current density for the N-DMC. (f) Charge/discharge retention at 20 A g^{-1} over 4000 cycles; inset: charge/discharge curves for the first and last few cycles.

that both the high surface area and the high N atom content enhanced the quadrupolar interactions of the N-DMC with CO_2 molecules.

The application of non-conductive frameworks can improve the efficiency of energy storage.[60] Herein, we examined the behavior of the CBF upon curing and activation, using a three-

electrode cell with 1.0 M KCl as a green medium. These conditions provided an extremely wide potential window range for cyclic voltammetry (CV; from −1.0 V to +1.0 V) for both samples. The CV curves of the CCBF [Fig. 7(b)] revealed the behavior of a very small electric double layer capacitor (EDLC). The activated conditions, however, provided a much higher area for the EDLC, compared to that under the cured conditions, at all of the tested scan rates [Fig. 7(a)]. For example, the capacitance at 5 mV s^{-1} was only 9 F g^{-1} after performing the curing process; in contrast, after activation, it reached 700 F g^{-1} at the same scan rate [Fig. 7(c)]. This enhancement in EDLC performance reflects the major effect of the carbonization technique: providing a higher surface area for electron transfer on the electrode surface. This behavior is also consistent with the increase in the surface area after the activation process. Therefore, the calculated integrated capacitances for the N-DMC after applying the activating conditions were over 60 times greater than those for the CCBF. The CV curves for the N-DMC possessed a quasi-rectangular shape, indicating a major EDLC performance. Supported by the XPS data, the CV curves of the N-DMC revealed a major EDLC with minor pseudocapacitance (PC) performance near −0.6 V, indicating the successful activation with N atoms (*e.g.*, pyridinic N and pyrrolic N) within the graphitic structure. Moreover, the insignificant PC representation indicates that lower degrees of functionalization occurred at the basal plane of the graphitic structure. This property is also unique to this approach, because the activation process was carefully performed under an inert atmosphere to allow hybridization with the N atoms inside the graphitic rings and to avoid severe functionalization with other defects in the periphery. These functionalities are known to enhance the electrochemical performance of electrode materials.[61] In addition, the charge/discharge curves, tested at various current densities (from 1.0 to 10.0 A g^{-1}) over the potential range of −1.0 to +1.0 V, are presented in Fig. 7(d). This potential range is the widest ever reported for an N-DMC; it provided capacitances of 185 F g^{-1} at 1.0 A g^{-1} and up to 121 F g^{-1} at 10.0 A g^{-1} [Fig. 7(e)]. The charge/discharge curves were all typically symmetrical at all of the investigated current densities. Moreover, the stability of the electrode was investigated at 20 A g^{-1} over 4000 cycles [Fig. 7(f)]. The average retention of the initial capacitance was 87% after 4000 cycles. In addition, the first and last few cycles of the charge/discharge cycles were almost identical and stable, with symmetrical shapes [inset to Fig. 7(f)]. Therefore, this N-DMC obtained directly from the CBF is a promising candidate material for energy storage applications; other porous carbons have not displayed such strong performance (Tables S2 and S3†).[62–71] As shown in Table S3,† these electrochemical results are considered much higher than other reported N-doped carbons. Therefore, we believe that our N-DMC is a promising candidate for efficient energy storage applications with an excellent performance. Moreover, this newly developed N-DMC could open the door for further investigation of triazine-based moieties as nitrogen-rich carbon sources for energy applications.

Conclusions

We have used both tri-functionalized phenolic and amine compounds, based on triazine units, to form a new covalent BZ framework that, after thermal ring opening, calcination, and KOH activation, converted into an N-doped microporous carbon based on triazine-functionalized polybenzoxazine. The obtained N-DMC possessed a spherical morphology, a large surface area (1469 m^2 g^{-1}), high thermal stability, and a high CO_2 adsorption capacity (7.46 mmol g^{-1} at 0 °C). In addition, the N-DMC displayed exceptional electrochemical performance during CV, with capacitances of 700 F g^{-1} at 5 mV s^{-1} and 185 F g^{-1} at 1.0 A g^{-1} in a three-electrode system. It also exhibited excellent stability performance, with an average retention of capacitance of 87% at 20 A g^{-1} after 4000 cycles. These characteristics confirm the efficiency of the activation procedure of this BZ prepolymer for various industrial applications.

Conflicts of interest

There are no conflicts to declare.

Acknowledgements

This study was supported financially by the Ministry of Science and Technology, Taiwan, under contracts MOST 106-2221-E-110-067-MY3 and 108-2218-E-110-013-MY3.

References

1 H. Ishida, in *Handbook of polybenzoxazine resins*, ed. H. Ishida and T. Agag, Elsevier, Amsterdam, 2011.
2 P. Froimowicz, L. Han, R. Graf, H. Ishida and C. R. Arza, *Macromolecules*, 2017, **50**, 9249–9256.
3 M. W. Wang, R. J. Jeng and C. H. Lin, *Macromolecules*, 2015, **48**, 530–535.
4 G. Kaya, B. Kiskan and Y. Yagci, *Macromolecules*, 2018, **51**, 1688–1695.
5 K. Zhang, L. Han, P. Froimowicz and H. Ishida, *Macromolecules*, 2017, **50**, 6552–6560.
6 C. F. Wang, Y. C. Su, S. W. Kuo, C. F. Huang, Y. C. Sheen and F. C. Chang, *Angew. Chem., Int. Ed.*, 2006, **45**, 2248–2251.
7 S. W. Kuo, Y. C. Wu, C. F. Wang and K. U. Jeong, *J. Phys. Chem. C*, 2009, **113**, 20666–20673.
8 H. C. Liu, W. C. Su and Y. L. Liu, *J. Mater. Chem.*, 2011, **21**, 7182–7187.
9 M. G. Mohamed and S. W. Kuo, *Polymers*, 2016, **8**, 225.
10 M. G. Mohamed and S. W. Kuo, *Macromol. Chem. Phys.*, 2019, **220**, 1800306.
11 N. N. Ghosh, B. Kiskan and Y. Yagci, *Prog. Polym. Sci.*, 2007, **32**, 1344–1391.
12 C. C. Yang, Y. C. Lin, P. I. Wang, D. J. Liaw and S. W. Kuo, *Polymer*, 2014, **55**, 2044–2050.

13 M. G. Mohamed, K. C. Hsu and S. W. Kuo, *Polym. Chem.*, 2015, **6**, 2423–2433.
14 H. K. Shih, C. C. Hsieh, M. G. Mohamed, C. Y. Zhu and S. W. Kuo, *Soft Matter*, 2016, **12**, 1847–1856.
15 S. Wang, W. C. Li, G. P. Hao, Y. Han, Q. Sun, X. Q. Zhang and A. H. Lu, *J. Am. Chem. Soc.*, 2011, **133**, 15304–15307.
16 G. P. Hao, W. C. Li, D. Qian, G. H. Wang, W. P. Zhang, T. Zhang, A. Q. Wang, F. Schuth, H. J. Bongard and A. H. Lu, *J. Am. Chem. Soc.*, 2011, **133**, 11378–11388.
17 Z. J. Zhao, M. R. H. S. Gilani, J. Lai, A. Nsabimana, Z. Liu, R. Luque and G. Xu, *Macromolecules*, 2018, **51**, 5494–5500.
18 M. Zhang, M. Chen, N. Reddeppa, D. Xu, Q. Jing and R. Zhang, *Nanoscale*, 2018, **10**, 6549–6557.
19 S. Gu, Z. Li, T. Miyoshib and S. Jana, *RSC Adv.*, 2015, **5**, 26801–26805.
20 L. Wan, J. Wang, Y. Sun, C. Feng and K. Li, *RSC Adv.*, 2015, **5**, 5331–5342.
21 L. Wan, J. Wang, C. Feng, Y. Sun and K. Li, *Nanoscale*, 2015, **7**, 6534–6544.
22 S. Wang, W. C. Li, L. Zhang, Z. Y. Jin and A. H. Lu, *J. Mater. Chem. A*, 2014, **2**, 4406–4412.
23 D. C. Guo, J. Mi, G. P. Hao, W. Dong, G. Xiong, W. C. Li and A. H. Lu, *Energy Environ. Sci.*, 2013, **6**, 652–659.
24 P. Wang, G. Zhang, Z. Li, W. Sheng, Y. Zhang, J. Gu, X. Zheng and F. Cao, *ACS Appl. Mater. Interfaces*, 2016, **8**, 26908–26915.
25 P. Thirukumaran, R. Atchudan, A. Parveen, Y. R. Lee and S. C. Kim, *J. Alloys Compd.*, 2018, **750**, 384–391.
26 L. Liu, Z. H. Xie, Q. F. Deng, X. X. Hou and Z. Y. Yuan, *J. Mater. Chem. A*, 2017, **5**, 418–425.
27 P. X. Hou, H. Orikasa, T. Yamazaki, K. Matsuoka, A. Tomita, N. Setoyama, Y. Fukushima and T. Kyotani, *Chem. Mater.*, 2005, **17**, 5187–5193.
28 X. Cui, Q. Yang, Y. Xiong, Z. Bao, H. Xing and S. Dai, *Chem. Commun.*, 2017, **53**, 4915–4918.
29 J. Kou and L. B. Sun, *Ind. Eng. Chem. Res.*, 2016, **55**, 10916–10925.
30 X. Zhang, K. Ma, M. Gan, G. Fu, M. Jin, Y. Lei, P. Yang and M. Yan, *J. Power Sources*, 2017, **340**, 22–31.
31 J. W. F. To, J. He, J. Mei, R. Haghpanah, Z. Chen, T. Kurosawa, S. Chen, W. G. Bae, L. Pan, J. B. H. Tok, J. Wilcox and Z. Bao, *J. Am. Chem. Soc.*, 2016, **138**, 1001–1009.
32 D. Xu, C. Chen, J. Xie, B. Zhang, L. Miao, J. Cai, Y. Huang and L. Zhang, *Adv. Energy Mater.*, 2016, **6**, 1501929.
33 J. Y. Wu, M. G. Mohamed and S. W. Kuo, *Polym. Chem.*, 2017, **8**, 5481–5489.
34 L. Hao, J. Ning, B. Luo, B. Wang, Y. Zhang, Z. Tang, J. Yang, A. Thomas and L. Zhi, *J. Am. Chem. Soc.*, 2015, **137**, 219–225.
35 W.-H. Li, K. Ding, H.-R. Tian, M.-S. B. Nath, W.-H. Deng, Y. Wang and G. Xu, *Adv. Funct. Mater.*, 2017, **27**, 1702067.
36 J. D. Moon and B. D. Freeman, *Nat. Mater.*, 2019, **18**, 92–93.
37 S. Wan, J. Guo, J. Kim, H. Ihee and D. Jiang, *Angew. Chem., Int. Ed.*, 2009, **48**, 5439–5442.
38 J. Tang, R. R. Salunkhe, J. Liu, N. L. Torad, M. Imura, S. Furukawa and Y. Yamauchi, *J. Am. Chem. Soc.*, 2015, **137**, 1572–1580.
39 R. R. Salunkhe, Y. V. Kaneti, J. Kim, J. H. Kim and Y. Yamauchi, *Acc. Chem. Res.*, 2016, **49**, 2796–2806.
40 F. K. Shieh, S. C. Wang, C. I. Yen, C. C. Wu, S. Dutta, L. Y. Chou, J. V. Morabito, P. Hu, M. H. Hsu, K. C. W. Wu and C. K. Tsung, *J. Am. Chem. Soc.*, 2015, **137**, 4276–4279.
41 C. Wu, Y. Liu, H. Liu, C. Duan, Q. Pan, J. Zhu, F. Hu, X. Ma, T. Jiu, Z. Li and Y. Zhao, *J. Am. Chem. Soc.*, 2018, **140**, 10016–10024.
42 S. Yan, X. Guan, H. Li, D. Li, M. Xue, Y. Yan, V. Valtchev, S. Qiu and Q. Fang, *J. Am. Chem. Soc.*, 2019, **141**, 2920–2924.
43 T. Zhou, S. Xu, Q. Wen, Z. Pang and X. Zhao, *J. Am. Chem. Soc.*, 2014, **136**, 15885–15888.
44 X. Feng, X. Ding and D. Jiang, *Chem. Soc. Rev.*, 2012, **41**, 6010–6022.
45 X. Zhuang, F. Zhang, D. Wu and X. Feng, *Adv. Mater.*, 2014, **26**, 3081–3086.
46 A. F. M. El-Mahdy, C. Young, J. Kim, J. You, Y. Yamauchi and S. W. Kuo, *ACS Appl. Mater. Interfaces*, 2019, **11**, 9343–9354.
47 A. F. M. El-Mahdy, C.-H. Kuo, A. A. Alshehri, J. Kim, C. Young, Y. Yamauchi and S.-W. Kuo, *J. Mater. Chem. A*, 2018, **6**, 19532–19541.
48 A. F. M. El-Mahdy, Y.-H. Hung, T. H. Mansoure, H.-H. Yu, T. Chen and S.-W. Kuo, *Chem. – Asian J.*, 2019, **14**, 1429–1435.
49 R. Gomes and A. A. Bhaumik, *RSC Adv.*, 2016, **6**, 28047–28054.
50 M. Baqar, T. Agag, R. Huang, J. Maia, S. Qutubuddin and H. Ishida, *Macromolecules*, 2012, **45**, 8119–8125.
51 G. Das, T. Skorjanc, S. K. Sharma, F. Gandara, M. Lusi, D. S. S. Rao, S. Vimala, S. K. Prasad, J. Raya, D. S. Han, R. Jagannathan, J. C. Olsen and A. Trabolsi, *J. Am. Chem. Soc.*, 2017, **139**, 9558–9565.
52 R. W. Tilford, S. J. Mugavero III, P. J. Pellechia and J. J. Lavigne, *Adv. Mater.*, 2008, **20**, 2741–2746.
53 L. M. Malard, M. A. Pimenta, G. Dresselhaus and M. S. Dresselhaus, *Phys. Rep.*, 2009, **473**, 51–87.
54 L. Shao, S. Wang, M. Liu, J. Huang and Y. N. Liu, *Chem. Eng. J.*, 2018, **339**, 509–518.
55 L. Liu, Y. Xia and J. Zhang, *RSC Adv.*, 2014, **4**, 59102–59105.
56 G.-P. Hao, W.-C. Li, D. Qian and A.-H. Lu, *Adv. Mater.*, 2010, **22**, 853–857.
57 L. Sun, C. Tian, Y. Fu, Y. Yang, J. Yin, L. Wang and H. Fu, *Chem. – Eur. J.*, 2014, **20**, 564–574.
58 H. M. Far, S. Donthula, T. Taghvaee, A. M. Saeed, Z. Garr, C. S. Leventis and N. Leventis, *RSC Adv.*, 2017, **7**, 51104–51120.
59 W. Xing, C. Liu, Z. Zhou, L. Zhang, J. Zhou, S. Zhuo, Z. Yan, H. Gao, G. Wang and S. Z. Qiao, *Energy Environ. Sci.*, 2012, **5**, 7323–7327.

60 L. Yu, L. Hu, B. Anasori, Y.-T. Liu, Q. Zhu, P. Zhang, Y. Gogotsi and B. Xu, *ACS Energy Lett.*, 2018, **3**, 1597–1603.
61 H. Liu, H. Song, X. Chen, S. Zhang, J. Zhou and Z. Ma, *J. Power Sources*, 2015, **285**, 303–309.
62 F. Qin, X. Tian, Z. Guo and W. Shen, *ACS Sustainable Chem. Eng.*, 2018, **6**, 15708–15719.
63 J. Zhang, W. Zhang, M. Han and J. Pang, *J. Mater. Sci.: Mater. Electron.*, 2018, **29**, 4639–4648.
64 J. Cao, C. J. Jafta, J. Gong, Q. Ran, X. Lin, R. Félix, R. G. Wilks, M. Bär, J. Yuan, M. Ballauff and Y. Lu, *ACS Appl. Mater. Interfaces*, 2016, **8**, 29628–29636.
65 J.-K. Ewert, D. Weingarth, C. Denner, M. Friedrich, M. Zeiger, A. Schreiber, N. Jäckel, V. Presser and R. Kempe, *J. Mater. Chem. A*, 2015, **3**, 18906–18912.
66 J. L. Goldfarb, G. Dou, M. Salari and M. W. Grinstaff, *ACS Sustainable Chem. Eng.*, 2017, **5**, 3046–3054.
67 Y. Lin, Z. Chen, C. Yu and W. Zhong, *ACS Sustainable Chem. Eng.*, 2019, **7**, 3389–3403.
68 T. Quan, N. Goubard-Bretesché, E. Härk, Z. Kochovski, S. Mei, N. Pinna, M. Ballauff and Y. Lu, *Chem. – Eur. J.*, 2019, **25**, 4757–4766.
69 D. C. Guo, J. Mi, G. P. Hao, W. Dong, G. Xiong, W. C. Li and A. H. Lu, *Energy Environ. Sci.*, 2013, **6**, 652–659.
70 T. Stimpfling and F. Leroux, *Chem. Mater.*, 2010, **22**, 974–987.
71 C.-M. Yang, Y.-J. Kim, J. Miyawaki, Y. A. Kim, M. Yudasaka, S. Iijima and K. Kaneko, *J. Phys. Chem. C*, 2015, **119**, 2935–2940.

